Inorganic Chemistry

Article

pubs.acs.org/IC

What Happens to $LiMnPO_4$ upon Chemical Delithiation?

Yiqing Huang,[†] Natasha A. Chernova,[†] Qiyue Yin,[‡] Qi Wang,[†] Nicholas F. Quackenbush,[§] Michal Leskes,[∥] Jin Fang,[†] Fredrick Omenya,[†] Ruibo Zhang,[†] Matthew J. Wahila,[§] Louis F. J. Piper,[§] Guangwen Zhou,[‡] Clare P. Grey,[∥] and M. Stanley Whittingham*[,†,⊥]

[†]Chemistry and Materials, [‡]Department of Mechanical Engineering & Materials Science and Engineering Program, [§]Department of Physics, Applied Physics, and Astronomy, and [⊥]NorthEast Center for Chemical Energy Storage (NECCES), Binghamton University, Binghamton, New York 13902, United States

[∥]Department of Chemistry, University of Cambridge, Lensfield Road, Cambridge CB2 1EW, United Kingdom

Supporting Information

ABSTRACT: Olivine $MnPO_4$ is the delithiated phase of the lithium-ion-battery cathode (positive electrode) material $LiMnPO_4$, which is formed at the end of charge. This phase is metastable under ambient conditions and can only be produced by delithiation of $LiMnPO_4$. We have revealed the manganese dissolution phenomenon during chemical delithiation of $LiMnPO_4$, which causes amorphization of olivine $MnPO_4$. The properties of crystalline $MnPO_4$ obtained from carbon-coated $LiMnPO_4$ and of the amorphous product resulting from delithiation of pure $LiMnPO_4$ were studied and compared. The phosphorus-rich amorphous phases in the latter are considered to be $MnHP_2O_7$ and $MnH_2P_2O_7$ from NMR, X-ray absorption spectroscopy, and X-ray photoelectron spectroscopy analysis. The thermal stability of $MnPO_4$ is significantly higher under high vacuum than at ambient condition, which is shown to be related to surface water removal.

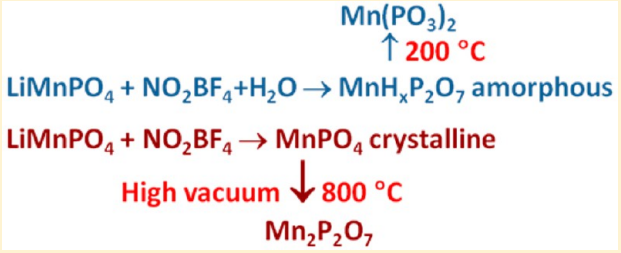

INTRODUCTION

Olivine-type $LiMPO_4$ (M = Fe, Mn, Co, and Ni) is a promising class of cathode materials for lithium-ion batteries.[1] $LiFePO_4$ is used as a power source for electric vehicles owing to its safety, long-term cycle life, and significantly improved power density. $LiMnPO_4$ could be a good substitute for commonly used cathode materials because it has higher voltage (4.1 V vs Li^+/Li) and higher energy density.[2−6] However, $LiMnPO_4$ has low electronic conductivity,[7] local structure distortion caused by Jahn−Teller active Mn^{3+} ions,[8−10] and a large cell volume change between $LiMnPO_4$ and $MnPO_4$ during the charge/discharge process,[11] along with a metastable delithiated phase.[12−15]

Safety is one of the most important criteria for commercialization of cathode materials, and the delithiated phases MPO_4 are relatively unstable compared to their lithiated forms, especially for Mn and Co.[16,17] These phases have not been synthesized directly so far, and chemical delithiation is the only method that allows investigation of the intrinsic thermal property of the materials without the influence of conductive agents and binders.[18] However, the chemical delithiation process corresponds to a potentiostatic (constant-voltage) charging, and the redox potentials of most commonly used oxidizing agents are higher than needed to oxidize $LiMPO_4$. Thus, sometimes the driving force for chemical delithiation is high enough to damage the MPO_4 structure.[19] Also, the mechanism of Li^+ and e^- transformation through chemical delithiation may be different from electrochemical delithiation, which is usually done at small constant current.[20,21]

We earlier reported the structural and thermal stability of crystalline $MnPO_4$ under ambient conditions and revealed the critical role of carbon coating.[22] We found an amorphous phase forming after chemical delithiation for $LiMnPO_4$ with no carbon. Such amorphization during chemical delithiation has also been reported by Yamada et al.,[5] Masquelier et al.,[7] and Park et al.[23] We also observed a significant water content, including surface water and crystalline water, in the delithiated products by thermogravimetric analysis (TGA)−mass spectrometry (MS). The crystalline $MnPO_4$ has ∼5% water, while the amorphous product has more than 15% water.

Here, the goal is to determine the inherent stability of olivine $MnPO_4$ and to understand how amorphization occurs upon chemical delithiation. Thus, we focus on the composition of the amorphous delithiated Li_xMnPO_4, as well as on the stability of crystalline $MnPO_4$ under high vacuum, where the surface water is removed. Because of the amorphous nature of the delithiation products, along with X-ray diffraction (XRD) and TGA−MS, we apply a variety of surface and local characterization techniques, including X-ray photoelectron spectroscopy (XPS), in situ X-ray absorption spectroscopy (XAS), in situ transmission electron microscopy (TEM), and NMR, to

Received: January 12, 2016
Published: April 11, 2016

DOI: 10.1021/acs.inorgchem.6b00089
Inorg. Chem. 2016, 55, 4335−4343

investigate the atomic and electronic structure of amorphous $MnPO_4$ and its stability.

EXPERIMENT

$LiMnPO_4$ was synthesized by a solid-state method at 600 °C with intermediate heating at 350 °C in a helium atmosphere from Li_2CO_3 (Fisher, ≥99%), $MnAc_2{\cdot}4H_2O$ (Aldrich, ≥99%), and $NH_4H_2PO_4$ (Aldrich, 99.99%) precursors. The details of the synthesis can be found elsewhere.[22] $LiMnPO_4$ so obtained is referred to as LMP-RC, where RC indicates residual carbon from carbonate and acetate precursors. The LMP-NC (no carbon) was synthesized by the same method, except that the final annealing was performed in an oxygen atmosphere at 600 °C.

$MnPO_4$ was obtained by chemical delithiation using NO_2BF_4 as the oxidizing reagent. A total of 800 mg of $LiMnPO_4$ was dispersed in 50 mL of acetonitrile, and then 3-fold excess NO_2BF_4 was added to the solution in a nitrogen-filled glovebox. The solution was stirred for 6 days, then filtered and washed with acetonitrile, ethanol, and acetone, and finally dried overnight.[22] The $MnPO_4$ samples are named following the names of their parent compounds by replacing LMP with MP.

The phase purity and crystal structure were characterized using powder XRD, where data were collected on a Scintag XDS2000 powder diffractometer equipped with a Ge(Li) solid-state detector and a Cu Kα sealed tube (λ = 1.54 Å). Rietveld refinement of the XRD patterns was performed using the *GSAS/EXPGUI* package.[24,25] In situ high-temperature XAS at Mn K-edge (6539 eV) was performed at the Advanced Photon Source, Beamline 5BM. MP-NC powder was diluted by boron nitride and pressed into a pellet of ∼1 cm diameter, which was loaded in a Linkam THMS600 heating stage for the heating experiment under the protection of an inert gas (nitrogen). Different heating rates were applied to the two regions: 5 °C/min over the temperature ranges of 25−100 and 200−300 °C and 2 °C/min over 100−200 °C. XAS data were collected at every 10 °C as the desired temperature was stabilized. XAS data were processed and analyzed using the *IFEFFIT* package.[26] The thermal properties of the samples were examined by TGA (PerkinElmer TGA 7). In a nitrogen atmosphere, the sample was heated to 100 °C at 5 °C/min and held for 16 h. Then the sample was continually heated to 600 °C at 5 °C/min, held for 1 h, and finally cooled to room temperature. The stoichiometries of Li, Mn, and P were determined by inductively coupled plasma optical emission spectrometry (ICP-OES; Varian Axial MPX).

XPS of $MnPO_4$ powders was performed using a Phi VersaProbe 5000 system with a monochromated Al Kα source and a hemispherical analyzer. The powders were pressed into pellets before the measurements to avoid the use of adhesive tape during the heating process. The core levels (Mn 2p, P 2p, O 1s, and C 1s) and the valence-band region were measured with a pass energy of 23.5 eV, corresponding to an instrumental resolution of 0.51 eV from analysis of both the Au $4f_{7/2}$ and Fermi edge of the gold foil. The binding-energy scale was calibrated to the C 1s core-level peak to account for sample charging effects. Following the initial XPS measurements, the samples were transferred to a heating stage in vacuo, heated from room temperature to 700 °C at a rate of 5 °C/min, and held at 700 °C for 30 min. The residual gases during the heating process were monitored using an SRS RGA200 mass spectrometer. Postheating XPS was then measured after the samples returned to room temperature. Finally, the samples were removed from the XPS chamber, and their XRD patterns were taken.

TEM samples were prepared by the powder sample preparation method with ultrasonic dispersion followed by drop casting onto a lacey carbon film supported by a TEM molybdenum grid purchased from Ted Pella, which was then mounted onto a Gatan heating holder with rapid heating capability using a Gatan hot-stage temperature controller. Structure and phase evolution were investigated by selected-area electron diffraction (SAED) on a JEOL JEM2100F transmission electron microscope operated at 200 kV. In order to minimize the beam effect, the electron dose was reduced during imaging. The diffraction patterns from different areas were taken during in situ heating to avoid the beam effect. The heating rates of MP-RC and MP-NC were 3 and 5 °C/min, respectively. For ex situ heating experiments, samples were heated from room temperature to 600 °C at a rate of 5 °C/min in air and held for 1 h. After cooling, SAED patterns of the products were taken to compare with the results of the in situ TEM heating experiments.

Solid-state NMR experiments[27] were performed on a Bruker Avance III 200 spectrometer using a Bruker 1.9 mm magic-angle-spinning (MAS) probe with MAS frequencies varying in the range 35−40 kHz. ^{1}H NMR spectra were acquired using a rotor-synchronized Hahn echo sequence with a radio-frequency (RF) pulse amplitude equal to 125 kHz. Resonances were referenced to adamantane set at 1.8 ppm. ^{31}P NMR spectra were acquired with a rotor-synchronized Hahn echo sequence as well as the projected−magic angle turning phase adjusted sideband separation (projection MATPASS) two-dimensional experiment for spinning sideband separation. For both experiments, a RF amplitude of 147 kHz was used and resonances were referenced to ammonium dihydrogen phosphate set at 0.8 ppm. Hahn echo spectra for MP-NC were acquired by summing four experiments with variable offsets (centered at 4500, 6000, 7500, and 9000 ppm) and 11 experiments for $MnHP_2O_7$ (offset varying from 0 to 10000 ppm in steps of 1000 ppm). Relaxation delays were optimized for each sample and nucleus and varied between 2 and 6 s for ^{1}H and between 10 and 50 ms for ^{31}P.

RESULTS AND DISCUSSION

The XRD patterns of the $LiMnPO_4$ samples (Figure S1) show a single phase with orthorhombic structure and unit cell parameters [a = 10.449(1) Å, b = 6.105(1) Å, and c = 4.746(1) Å] that are similar for $LiMnPO_4$ both with residual carbon and with no carbon (Table S1). The cell volumes are close to the literature value of 303.2 Å^3.[28] The XRD patterns (Figure 1) of chemically delithiated samples reveal the olivine $MnPO_4$ phase in MP-RC, with a small amount of the $Mn_2P_2O_7$ phase present in some samples. Rietveld refinement (Table S1) shows that the unit cell parameter of MP-RC is similar to that of our previous work.[22] According to our previous study,[22] the residual carbon content is ∼0.3 wt %. In contrast, MP-NC is basically amorphous with some weak and broad peaks of $MnPO_4$ recognizable in the XRD pattern. Such amorphous nature of MP-NC is also confirmed by TEM (Figure 2).

The composition of the delithiation products determined by ICP-OES (Table 1) shows that there is no lithium in either MP-RC or MP-NC; however, manganese deficiency is observed in both samples. Such manganese deficiency may indicate the existence of a second phosphorus-rich amorphous phase.

One of the most possible reasons for manganese deficiency is manganese dissolution into the solvent during chemical delithiation. ICP-OES was used to analyze the element concentration in the solutions that remained after this process. We collected the original solvent solution (called original). Then we used acetonitrile, ethanol, and acetone to wash the samples and collected this portion of the solution (called wash) as well. According to the ICP results (Table 2), the element concentration in the wash solution is 1 order of magnitude less than that in the original solution, so dissolution occurs upon chemical delithiation, while the influence of the subsequent wash is negligible. It is also interesting to note that, in the case of MP-RC, manganese and phosphorus are being dissolved in a ratio of 1.34:1, while from MP-NC, more than three manganese atoms per phosphorus are dissolved. This is consistent with the higher manganese deficiency found in the MP-NC sample. Furthermore, we observe that the crystallinity of $MnPO_4$ diminishes as the manganese deficiency increases.

DOI: 10.1021/acs.inorgchem.6b00089
Inorg. Chem. 2016, 55, 4335−4343

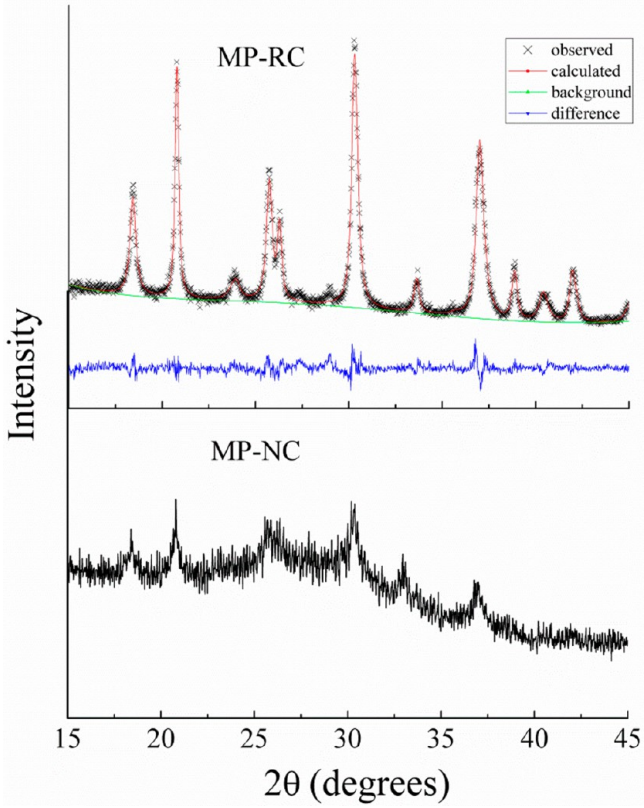

Figure 1. XRD patterns and Rietveld refinement of MP-RC (top) and XRD patterns of MP-NC (bottom).

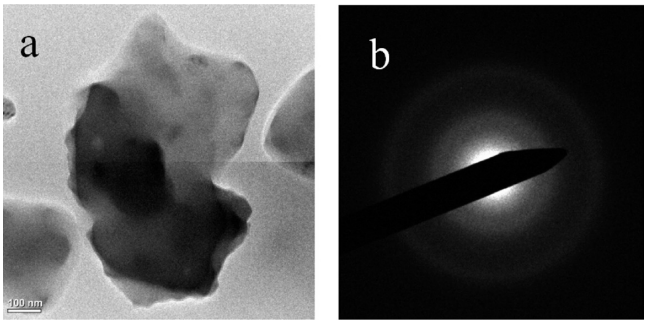

Figure 2. (a) TEM image and (b) electron diffraction pattern of MP-NC.

Table 1. ICP Results of MP-RC and MP-NC

	Li/Mn/P ratio
MP-RC	0.00:0.84:1.00
MP-NC	0.00:0.65:1.00

Table 2. ICP Results of Chemical Delithiation and Washing Solutions

	manganese (ppm)	phosphorus (ppm)	Mn/P molar ratio
MP-RC original	39.59	16.69	1.34:1
MP-RC wash	1.45	1.12	
MP-NC original	23.90	4.29	3.14:1
MP-NC wash	1.21	1.95	

To further understand the nature of the delithiated products, we used an XPS technique to investigate their surface composition, manganese oxidation states, and electronic structures. Figure 3 shows the Mn 2p, C 1s, and valence-band XPS spectra collected from the MP-RC and MP-NC samples. The C 1s spectra show the typical surface carbon species centered around 285 eV in both samples, as well as a small peak at higher binding energy representative of the residual carbon only seen in the MP-RC spectra. In the Mn 2p core-level spectra, the main Mn $2p_{3/2}$ peak is at 642 eV, representing Mn^{3+}, while an additional shoulder at lower binding energy is observed for MP-NC. This indicates that manganese has mixed valences of 2+ and 3+ in MP-NC, while MP-RC shows mainly Mn^{3+}. This is in agreement with the XAS results (Figure S2) to be discussed in detail later. From analysis of the core-level XPS, the atomic composition at the surface shows manganese deficiency and no litihum in both MP-RC and MP-NC, which is in good agreement with the ICP-OES results. The valence band of MP-RC most closely resembles that of the pure crystalline phase $MnPO_4$, although the features are less pronounced, as is expected. In the valence-band spectra of MP-NC, there is a feature at ~15 eV, which is less pronounced in MP-RC. This is a key signature of the pyrophosphate phase.[22] This is evidence that some pyrophosphate species may exist in the amorphous phase.

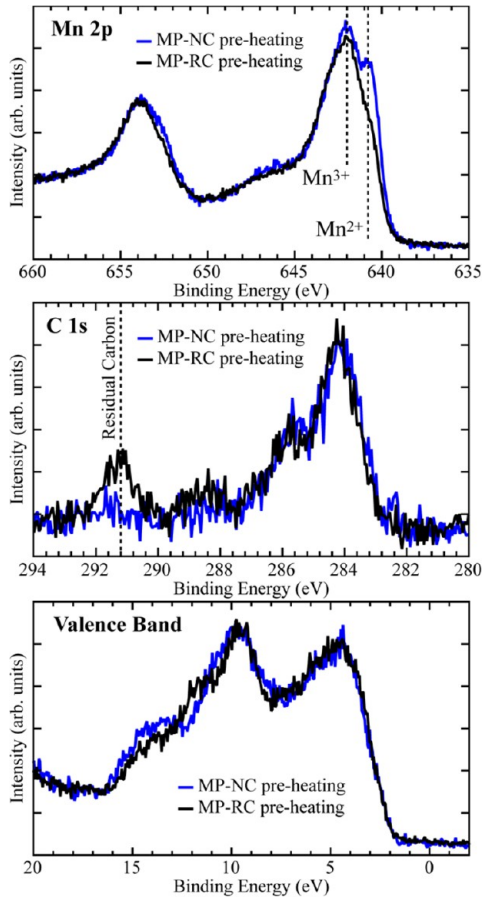

Figure 3. Mn 2p, C 1s, and valence-band XPS of MP-RC and MP-NC.

According to the TGA–MS experiments in our previous study,[22] upon heating, MP-RC and MP-NC show abnormal weight loss (about 10 and 20 wt %, respectively), with two peaks related to water loss occurring at 100 and 300 °C. Thus, here we aim to investigate the nature of water (or protons) in the samples and to understand their influence on the

DOI: 10.1021/acs.inorgchem.6b00089
Inorg. Chem. 2016, 55, 4335–4343

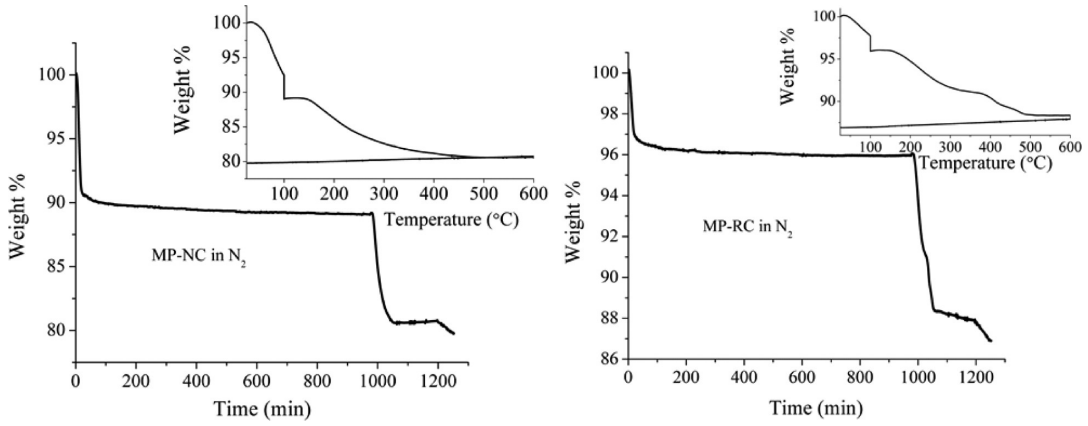

Figure 4. Thermal data upon heating the MP-NC (left) and MP-RC (right) samples in a nitrogen atmosphere at a rate of 5 °C/min to 100 °C, holding for 16 h, then heating to 600 °C, holding for 2 h, and finally cooling to room temperature.

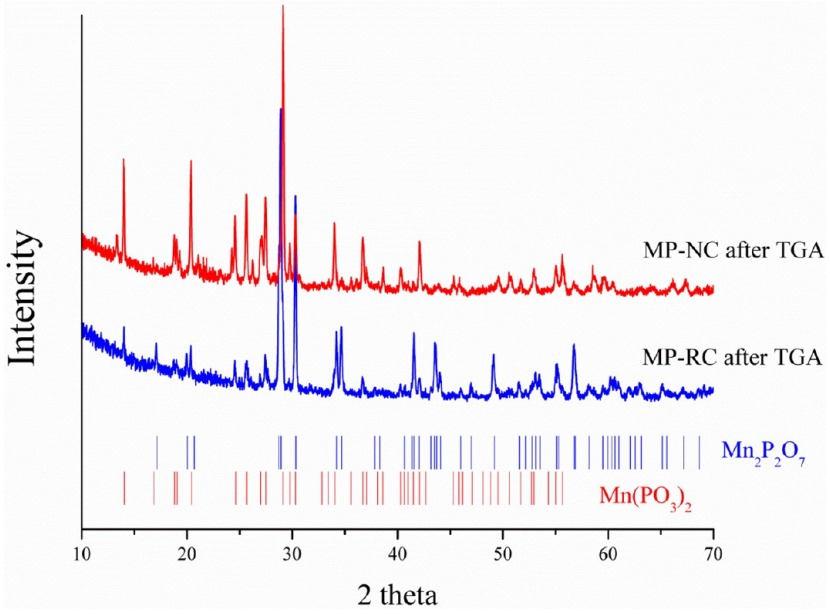

Figure 5. XRD patterns of the decomposition products of MP-RC and MP-NC after TGA.

decomposition routes of MP-RC and MP-NC. We believe that both are keys to understanding the amorphous phase in the MP-NC sample. First, we have quantified the amounts of surface water and structural water using TGA with a long hold at 100 °C (Figure 4). We use "structural water" here as an umbrella term, keeping in mind that it could also be protons or hydroxyl groups. For MP-NC, the total weight loss is 20%, and 10% happens at 100 °C. For MP-RC, the total weight loss is 12%, and 4% takes place at 100 °C. This indicates that the MP-NC sample has absorbed more total water and also has a larger amount of structural water than the carbon-containing MP-RC.

Second, we took XRD patterns of the compounds after TGA, which are the final decomposition products of MP-RC and MP-NC (Figure 5). Both of them are a mixture of $Mn_2P_2O_7$ and $Mn(PO_3)_2$. The product of MP-RC is majorly $Mn_2P_2O_7$, 75 wt % according to Rietveld refinement, while the product of MP-NC is majorly $Mn(PO_3)_2$ (60 wt %). This suggests the existence of two phases in both delithiated products; then $Mn_2P_2O_7$ is formed from $MnPO_4$ decomposition, as was previously reported,[22] and $Mn(PO_3)_2$ is due to amorphous phase decomposition. It is also consistent with the element ratio: a mixture of $Mn_2P_2O_7$ and $Mn(PO_3)_2$ would give a Mn/P ratio between 0.5 and 1.

Led by clues that the amorphous phase is likely to be a pyrophosphate and its decomposition products are $Mn(PO_3)_2$ and water, we searched the PDF4+ database and identified the most likely candidate as $MnHP_2O_7$. We have synthesized this compound as described in the Supporting Information and confirmed that its decomposition product is, in fact, $Mn(PO_3)_2$, as was previously reported.[29] We then used this $MnHP_2O_7$ along with other manganese compounds containing the (pyro)phosphate group and water or protons ($MnPO_4{\cdot}H_2O$ and $Mn_2P_2O_7$; Figure S3) to investigate the amorphous product using local techniques: ^{31}P and ^{1}H NMR and XAS at Mn K-edge.

The ^{31}P NMR resonance frequency is dominated by the Fermi–contact interaction, which is specific to the transition-metal-ion coordination shell around the nucleus.[30] The exact shift depends on the transition-metal oxidation state as well as the bond geometry. Furthermore, the resonances are broadened by the dipolar interaction between the unpaired electrons and detected nucleus. This spectral broadening can be

DOI: 10.1021/acs.inorgchem.6b00089
Inorg. Chem. 2016, 55, 4335–4343

reduced to some extent by MAS by breaking the resonance into an isotropic line and a manifold of spinning sidebands (Figure 6; Hahn echo spectra in black). The 2D projection MATPASS

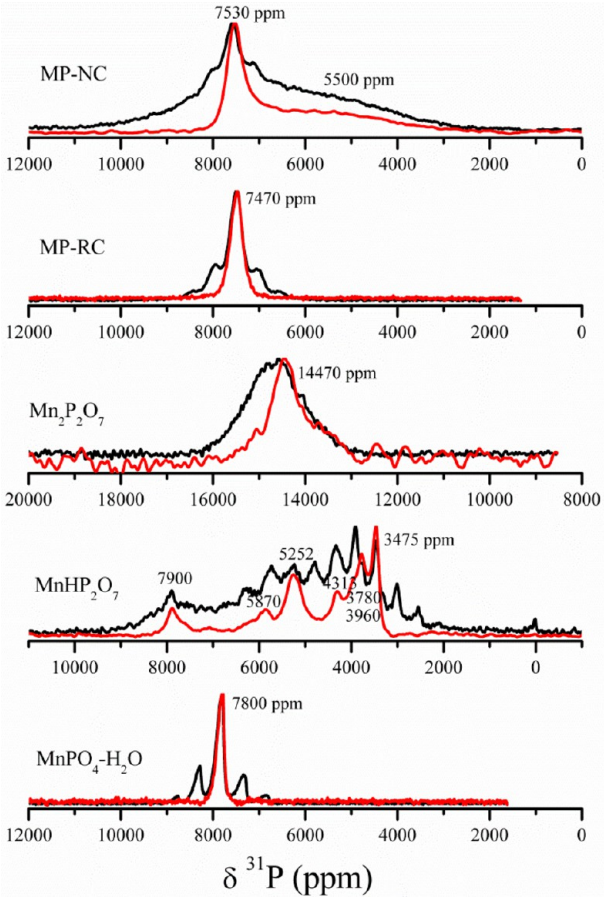

Figure 6. ^{31}P MAS NMR spectra of MP-RC, MP-NC, $Mn_2P_2O_7$, $MnHP_2O_7$, and $MnPO_4{\cdot}H_2O$ at room temperature. Hahn echo spectra are shown in black, while the isotropic rows from a 2D projection MATPASS experiment are shown in red.

is used here to separate the spinning sidebands from the isotropic resonances, resulting in the isotropic spectrum (Figure 6, red), which can be used to identify ^{31}P in different environments. The ^{31}P NMR spectrum (Figure 6) of MP-RC displays a single resonance at ~7500 ppm, which is the main PO_4 resonance. The spectrum of MP-NC shows the same environment at ~7500 ppm as that for MP-RC and a second broad resonance between 3000 and 7000 ppm. The width of this resonance, even in the isotropic spectrum, can be the result of multiple overlapping ^{31}P disordered environments. The region of this broad resonance overlaps with some of the resonances observed for $MnHP_2O_7$.

The ^1H MAS NMR spectra of all samples contain two sharp resonances at 2 and 7 ppm (Figure 7). Because these resonances are very sharp and have relatively long spin−lattice relaxation (about 1 s), we believe that the corresponding H atoms are not coordinated to Mn ions but could be due to some mobile surface species. Additional broader resonances that are also shifted outside the standard chemical shift range of ^1H are observed for $MnPO_4{\cdot}H_2O$ (at −9.3 ppm) and $MnHP_2O_7$ (29 and 15 ppm). These could correspond to nonmobile H atoms in closer proximity to manganese. The ^1H NMR spectrum of MP-NC has a broad contribution at 15−30

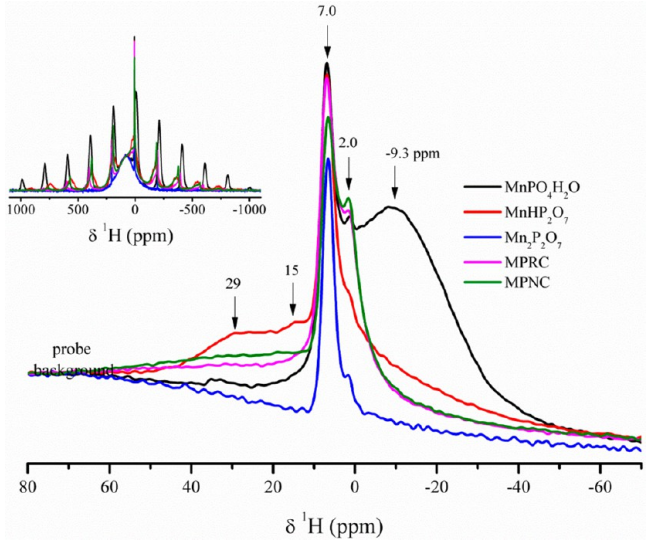

Figure 7. ^1H MAS NMR Hahn echo spectra of MP-RC, MP-NC, $Mn_2P_2O_7$, $MnHP_2O_7$, and $MnPO_4{\cdot}H_2O$ at room temperature, with a zoom on the isotropic region (normalized by the probe background signal at ~100 ppm). The full spectra are shown in the inset.

ppm (above the probe background signal and more clearly seen in the sideband region in the inset), which may be due to the contribution of structural hydrogen in MP-NC and is slightly more significant than that for MP-RC. Thus, ^{31}P and ^1H MAS NMR spectra suggest that the amorphous phase in MP-NC is similar to that in $MnHP_2O_7$. However, because the manganese oxidation state is between 2+ and 3+, MP-NC could be a mixture of $MnHP_2O_7$ and $MnH_2P_2O_7$. Figure S4 shows the structures of $MnHP_2O_7$ and $MnH_2P_2O_7$.

Furthermore, we have performed a high-temperature in situ XAS experiment on MP-NC to study the phase transformation upon temperature change. Two regions of changes were observed by analysis of Mn K-edge by XAS. The first process (20−100 °C) only involves the elimination of surface ligands, especially the removal of adsorbed water, which is evidenced by the gradual decrease in the intensity of the main absorption peak along with a slight downshift of the edge position as the temperature increases from 20 to 100 °C (Figure 8a).

As the temperature rises above 100 °C, temperature-induced transformation in the sample is reflected by spectral changes in Figure 8b. Specifically, the absorption edge shifts to a lower energy accompanied by a significant increase in the intensity of the main absorption peak. This finding by XANES suggests that manganese is being reduced upon heating, and such a reduction of the manganese valence is closely associated with the change of the local environment around the element. On the other hand, the evolution of the manganese local structure caused by thermal treatment is documented in the concurrently collected EXAFS data. Inspecting the radial distribution function of manganese obtained from Fourier-transformed EXAFS, we observe the most noticeable change in the r range of 1−2 Å, where the peak(s) predominantly feature the interaction between manganese and its nearest-neighboring atoms (oxygen). As demonstrated, the split peaks exhibited by MP-NC at 100 °C and lower temperatures gradually converge and eventually at 300 °C become one sharp band at a relatively longer distance.

This transformation of the Mn−O bonds was further confirmed by quantitative analysis by structure modeling of

DOI: 10.1021/acs.inorgchem.6b00089
Inorg. Chem. 2016, 55, 4335−4343

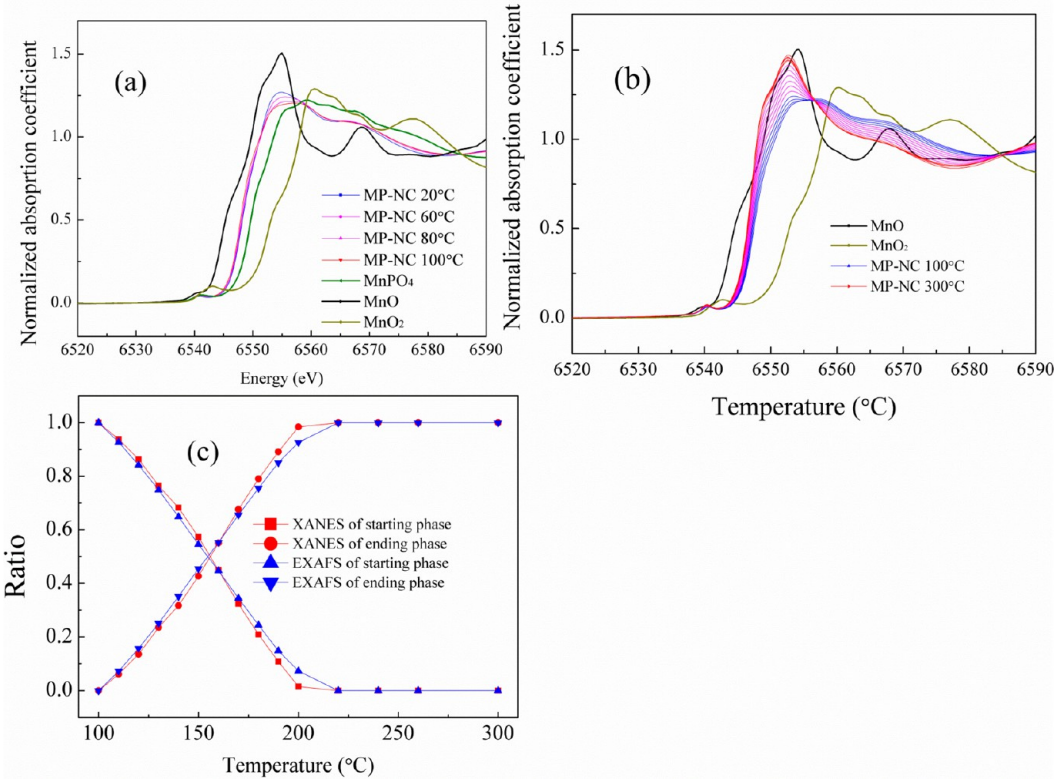

Figure 8. In situ XAS at Mn K-edge of MP-NC: (a) XANES between room temperature and 100 °C; (b) XANES between 100 and 300 °C; (c) mixing fraction of the start and end phases during thermal treatment of MP-NC. LCF on Mn K-edge: (red) XANES (energy region 6528.5−6578.5 eV); (blue) EXAFS in k space: k_w = 2; k range of 3−12.

EXAFS data of the MP-NC sample. Fitting results (Table S2 and Figure S5) reveal that, in the MP-NC sample of 100 °C, manganese is coordinated by oxygen at two different distances: 1.87 ± 0.02 and 2.09 ± 0.03 Å. The calculated coordination numbers (CNs) are 2.4 ± 0.6 and 2.2 ± 0.6, respectively. In contrast, upon thermal treatment, the first coordination shell of manganese in the sample can be characterized by hexacoordinating oxygen (CN = 6.5 ± 0.7) at a distance of 2.10 ± 0.01 Å. For the latter case, a Mn−Mn bond with CN = 2 and the calculated distance of 3.42 ± 0.03 Å, is required to fit the EXAFS data at a higher r range, which is consistent with the proposed structure of $Mn(PO_3)_2$. This subtle discrepancy between the two data provides more direct evidence for transformation of the structure.

The spectral features remain the same as the sample is cooled from 300 to 25 °C, indicating an irreversible transformation. In addition, both XANES and EXAFS data of the temperature series exhibit multiple isosbestic points, suggesting chemical transformation is a direct reaction of two phases: MP-NC → $Mn(PO_3)_2$. Consistent results were obtained as a linear composition fit (LCF) was applied to XANES and EXAFS data (Figure 8c). One concludes that, with a temperature increase, MP-NC is gradually converted to $Mn(PO_3)_2$. The phase transformation completes at a temperature slightly above 200 °C, and no significant change is involved as the temperature is raised further.

As we mentioned before, upon heating, the loss of water leads to structural disorder and phase transformation, which decreases the thermal stability of both MP-RC and MP-NC. However, if we perform the heating process under high vacuum, where surface water has been removed before heating, the thermal stability of MP-RC and MP-NC could be increased.

To further investigate the thermal stability of MP-RC and MP-NC under high vacuum, the XRD and XPS spectra of the samples before and after high vacuum heating are compared. From the XRD data (Figure 9), we can find that the major

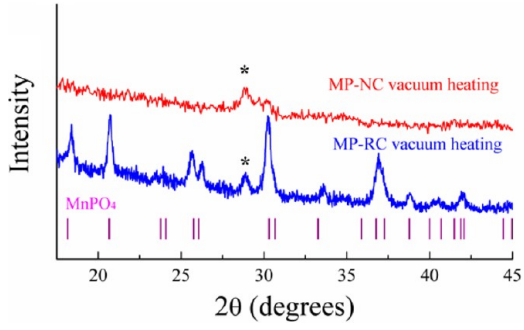

Figure 9. XRD patterns of the products of MP-RC and MP-NC after heating at 700 °C under high vacuum.

phase of MP-RC did not change after vacuum heating. However, the relative intensity of the 29° peak (asterisk) increased, which is a characteristic peak of $Mn_2P_2O_7$. Also, we can see the 29° peak of the MP-NC sample appearing after heating, suggesting that both MP-RC and MP-NC have been partially decomposed upon heating. When the XPS before and after high-vacuum heating (Figure 10) are compared, it can be seen that the Mn^{2+} peak became stronger in both MP-RC and MP-NC postheating. This indicates that the samples started to decompose and some $Mn_2P_2O_7$ was formed. The valence band also shows an increase in features associated with the pyrophosphate phase; the most noticeable signature is the

DOI: 10.1021/acs.inorgchem.6b00089
Inorg. Chem. 2016, 55, 4335−4343

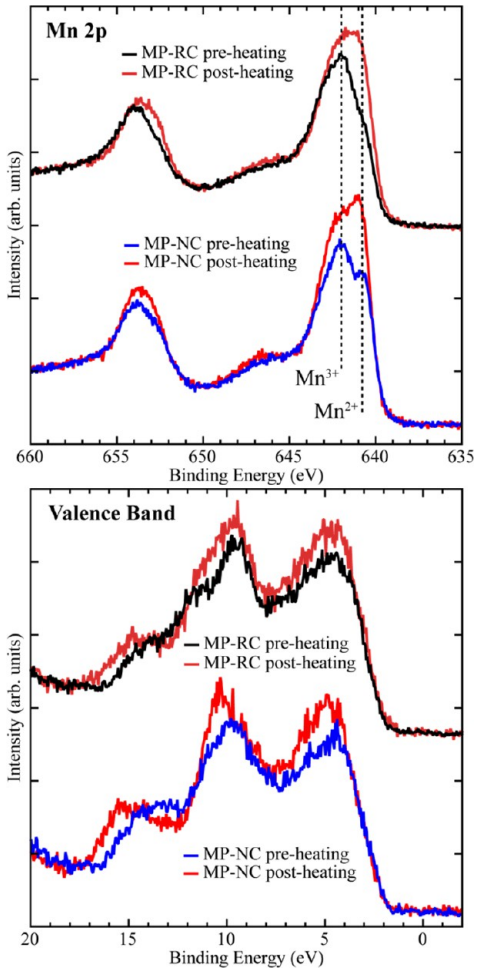

Figure 10. Mn 2p and valence-band XPS of MP-RC and MP-NC before and after annealing under high vacuum.

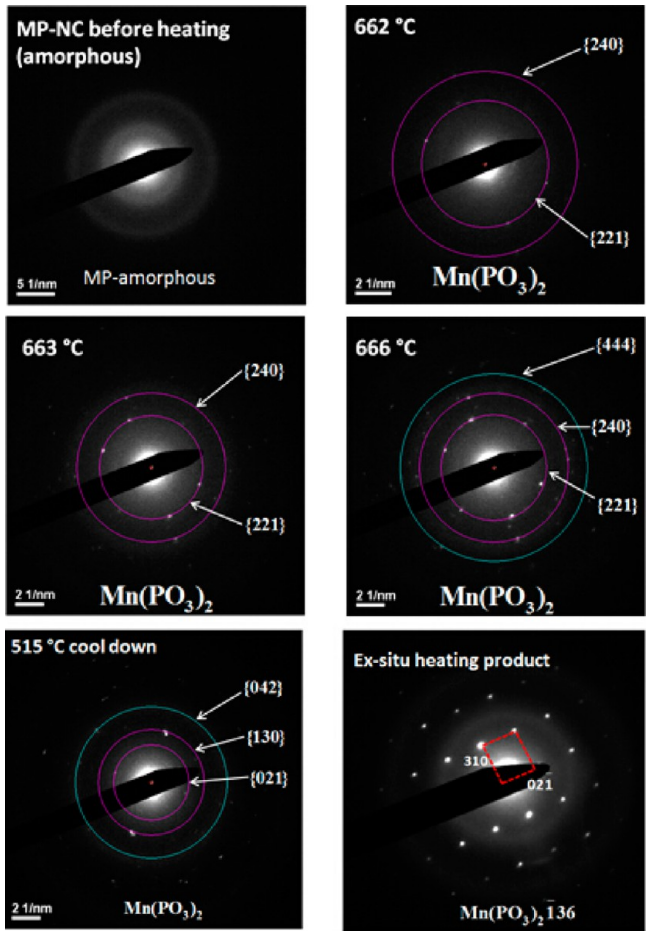

Figure 11. High-temperature in situ electron diffraction patterns of MP-NC.

feature near 15 eV. No change was observed in the C 1s region except for a reduction of the intensity of the surface carbon peaks. Combining the XRD and XPS results, we conclude that both MP-RC and MP-NC partially decompose at 700 °C under high vacuum. This shows that their thermal stability under high vacuum is much higher than that under ambient conditions, considering that the decomposition temperature of MP-RC is only 400 °C in the latter case.

To confirm the thermal stability of MP-RC and MP-NC under high vacuum, we have used high-temperature in situ TEM diffraction to study the phase transformation from room temperature to 800 °C. According to Figure 11, initially MP-NC is amorphous. The first diffraction pattern appears at around 660 °C and is identified as $Mn(PO_3)_2$. After cooling, the in situ diffraction pattern is also identified as $Mn(PO_3)_2$, except that the orientation changed. Similarly, SAED shows that the phase of the ex situ heating product is also $Mn(PO_3)_2$, with single-crystal spot patterns. As the ex situ product is held at 600 °C for 1 h, a higher crystallinity is expected.

Figure S6 shows a typical index diagram of the SAED pattern of MP-RC. In the in situ heating process (Figure 12), the starting material is polycrystalline $MnPO_4$, and the phase transformation does not occur until about 790 °C, where we first identify a $Mn_2P_2O_7$ pattern. To avoid the beam effect, diffraction patterns were taken from other areas of the sample, and they confirm the phase transformation, as shown by the diffraction pattern indexed as $Mn_2P_2O_7$ [001] at 800 °C, which remains stable after cooling. TEM diffraction proves that the in situ heated product is the same as the ex situ heated product. On the other hand, the intermediate-phase sarcopside $Mn_3(PO_4)_2$ was not observed. It could just be indistinguishable because of the fact that the 020 spacing of $Mn_3(PO_4)_2$ is so close to the 110 spacing of $Mn_2P_2O_7$ ($d[Mn_3(PO_4)_2\ (020)] = 0.502$ nm; $d[Mn_2P_2O_7(110)] = 0.517$ nm). Alternatively, the high-vacuum condition could remove the surface species of the sample, then minimize the structure disorder, and suppress the formation of sarcopside $Mn_3(PO_4)_2$.

Finally, putting together the results of various techniques, we propose that, during the chemical delithiation of $LiMnPO_4$, an amorphous phase is formed, which is a mixture of $MnHP_2O_7$ and $MnH_2P_2O_7$ (named as $MnH_yP_2O_7$, where $1 < y < 2$). Such an amorphous phase is formed by the following side reaction:

$$2LiMnPO_4 + 4NO_2BF_4 + (1 + 0.5y)H_2O \rightarrow MnH_yP_2O_7 + Mn(NO_3)_2 + 2BF_3 + 2HF + 0.25yO_2 + 2LiBF_4 + 2NO_2$$

$MnH_yP_2O_7$ and $MnPO_4$ are the two end members of the chemical delithiation process. If $LiMnPO_4$ is well carbon-coated and delithiated under perfect conditions (oxygen- and moisture-free), the product should be pure $MnPO_4$. However, if $LiMnPO_4$ is not protected by carbon or delithiated in a relatively high-moisture-level condition, the product would be a

DOI: 10.1021/acs.inorgchem.6b00089
Inorg. Chem. 2016, 55, 4335−4343

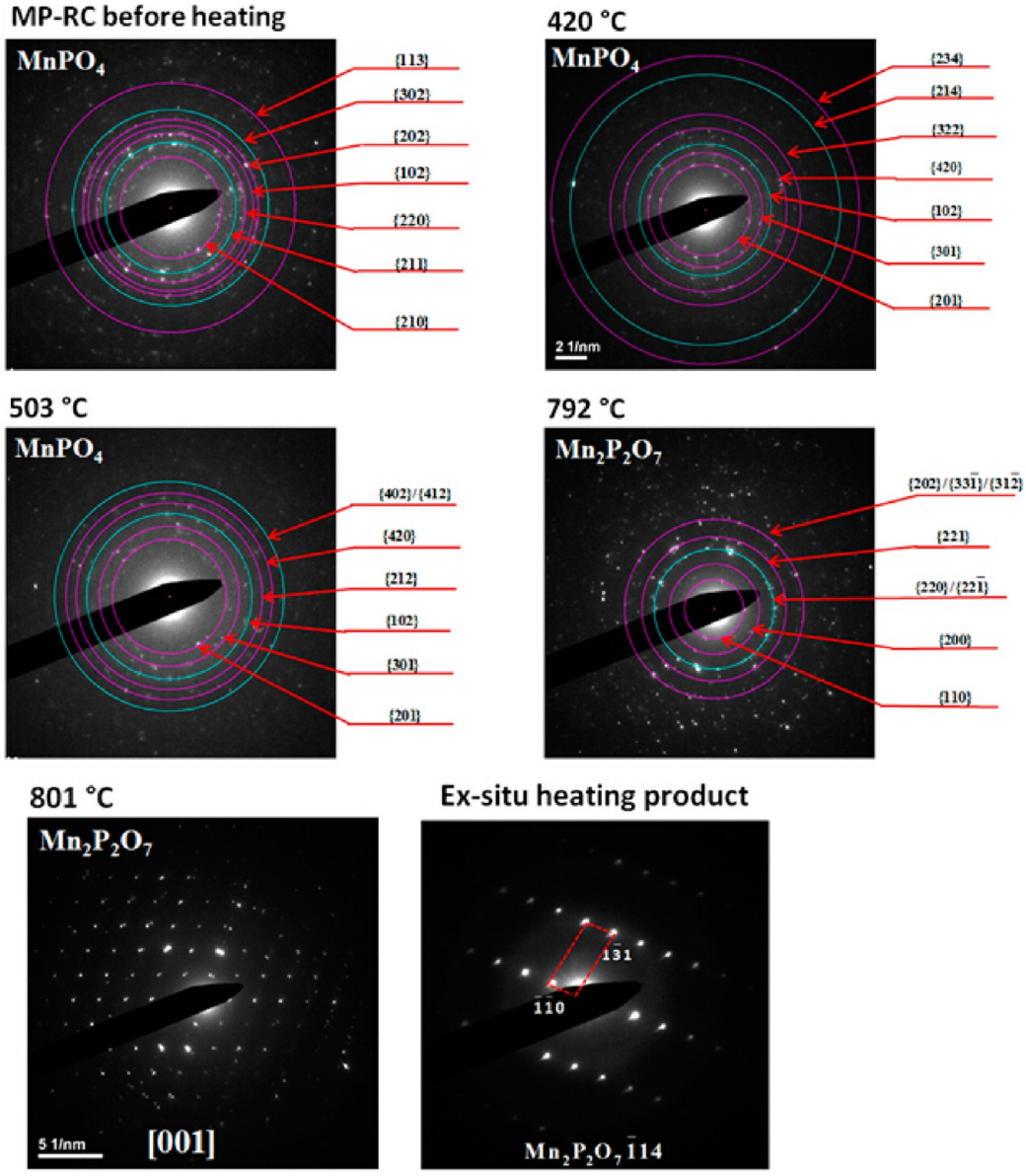

Figure 12. High-temperature in situ electron diffraction patterns of MP-RC.

mixture of $MnH_yP_2O_7$ and $MnPO_4$. In the worst case, it becomes completely amorphous $MnH_yP_2O_7$ (MP-NC). Thus, MP-RC ($Mn_{0.84}PO_4$) can be considered as major $MnPO_4$ with minor $MnH_yP_2O_7$, while MP-NC ($Mn_{0.65}PO_4$) can be considered as minor $MnPO_4$ with major $MnH_yP_2O_7$. Thermal decomposition of $MnHP_2O_7$ and $MnH_2P_2O_7$ should follow these reactions:

$$MnHP_2O_7 \rightarrow Mn(PO_3)_2 + 0.25O_2 + 0.5H_2O$$

$$MnH_2P_2O_7 \rightarrow Mn(PO_3)_2 + H_2O$$

The side reaction with water possible upon chemical delithiation compromises the thermal stability of $MnPO_4$ and possibly its other properties. Even if the XRD pattern of chemically delithiated $MnPO_4$ shows a pure phase, it possibly contains a certain amount of amorphous-phase $MnH_yP_2O_7$. The easiest test to determine the degree of amorphization is TGA with the following XRD analysis of the products. Residual water present in electrochemical cells is also expected to influence the electrochemical behavior of the $LiMnPO_4$ cathode. On the positive side, we have shown that $MnPO_4$ is much more stable than was previously reported if contact with a humid environment is avoided.

CONCLUSION

Analysis of the chemical delithiation products of $LiMnPO_4$ and their thermal decomposition products by XRD, XAS, XPS, and TEM has revealed the mechanism of chemical delithiation of $LiMnPO_4$ and the thermal stability of its products. During chemical delithiation, $MnPO_4$ suffers from a side reaction with residual water in the solvent. This results in structural disorder and partial manganese dissolution into the solvent, eventually leading to amorphization. The extent of this side process depends on the water content and on whether the surface is carbon-coated or not. Carbon-coated $LiMnPO_4$ mostly forms olivine $MnPO_4$ upon chemical delithiation. The amorphous phase prevailing in the delithiation products of noncoated $LiMnPO_4$ has a different composition from olivine $MnPO_4$ and is even more hygroscopic. This amorphous phase is a mixture

DOI: 10.1021/acs.inorgchem.6b00089
Inorg. Chem. 2016, 55, 4335−4343

of $MnHP_2O_7$ and $MnH_2P_2O_7$, and it starts to decompose to $Mn(PO_3)_2$ at 100 °C. However, under high-vacuum conditions, both olivine $MnPO_4$ and the amorphous phase show significantly higher thermal stability than that at ambient conditions. Olivine $MnPO_4$ decomposes at 800 °C under high vacuum, in contrast to the decomposition temperature of 400 °C at ambient conditions, while the amorphous phase decomposes to $Mn(PO_3)_2$ at 660 °C. Such increased thermal stability is shown to be related to surface water removal at the high-vacuum condition.

■ ASSOCIATED CONTENT

Supporting Information

The Supporting Information is available free of charge on the ACS Publications website at DOI: 10.1021/acs.inorgchem.6b00089.

XRD patterns and Rietveld refinement of LMP-RC and LMP-NC, lattice parameters of $LiMnPO_4$ and $MnPO_4$, XANES spectra of $MnPO_4$ and reference materials, synthesis methods of NMR standards $MnPO_4{\cdot}H_2O$, $Mn_2P_2O_7$, and $MnHP_2O_7$ and their diffraction patterns, structures of $MnHP_2O_7$ and $MnH_2P_2O_7$, results of EXAFS analysis of amorphous $MnPO_4$ upon heating, and the typical index diagram of the SAED pattern of MP-RC (PDF)

■ AUTHOR INFORMATION

Corresponding Author

*E-mail: stanwhit@gmail.com.

Notes

The authors declare no competing financial interest.

■ ACKNOWLEDGMENTS

This work was supported as part of the NECCES, an Energy Frontier Research Center funded by the U.S. Department of Energy (DOE), Office of Science, Basic Energy Sciences, under Award DE-SC0012583. Q.W. was supported at Brookhaven National Laboratory by NYSERDA and NYSTAR with matching funds for NECCES. TEM work was carried out at the Center for Functional Nanomaterials, Brookhaven National Laboratory, which is supported by the U.S. DOE, Office of Basic Energy Sciences, under Contract DE-SC0012704. This research used resources of the Advanced Photon Source, a U.S. DOE, Office of Science, user facility operated for the U.S. DOE, Office of Science, by Argonne National Laboratory under Contract DE-AC02-06CH11357.

■ REFERENCES

(1) Padhi, A. K.; Nanjundaswamy, K. S.; Goodenough, J. B. *J. Electrochem. Soc.* **1997**, *144*, 1188−1194.
(2) Whittingham, M. S. *Chem. Rev.* **2004**, *104*, 4271−4301.
(3) Whittingham, M. S. *Chem. Rev.* **2014**, *114*, 11414−11443.
(4) Li, G.; Azuma, H.; Tohda, M. *Electrochem. Solid-State Lett.* **2002**, *5*, A135−A137.
(5) Yamada, A.; Chung, S. C. *J. Electrochem. Soc.* **2001**, *148*, A960−A967.
(6) Kim, S. W.; Kim, J.; Gwon, H.; Kang, K. *J. Electrochem. Soc.* **2009**, *156*, A635−A638.
(7) Delacourt, C.; Laffont, L.; Bouchet, R.; Wurm, C.; Leriche, J. B.; Morcrette, M.; Tarascon, J. M.; Masquelier, C. *J. Electrochem. Soc.* **2005**, *152*, A913−A921.
(8) Nie, Z. X.; Ouyang, C. Y.; Chen, J. Z.; Zhong, Z. Y.; Du, Y. L.; Liu, D. S.; Shi, S. Q.; Lei, M. S. *Solid State Commun.* **2010**, *150*, 40−44.
(9) Ong, S. P.; Chevrier, V. L.; Ceder, G. *Phys. Rev. B: Condens. Matter Mater. Phys.* **2011**, *83*, 075112.
(10) Piper, L. F. J.; Quackenbush, N. F.; Sallis, S.; Scanlon, D. O.; Watson, G. W.; Nam, K. W.; Yang, X. Q.; Smith, K. E.; Omenya, F.; Chernova, N. A.; Whittingham, M. S. *J. Phys. Chem. C* **2013**, *117*, 10383−10396.
(11) Meethong, N.; Huang, H. Y. S.; Speakman, S. A.; Carter, W. C.; Chiang, W. M. *Adv. Funct. Mater.* **2007**, *17*, 1115−1123.
(12) Ong, S. P.; Jain, A.; Hautier, G.; Kang, B.; Ceder, G. *Electrochem. Commun.* **2010**, *12*, 427−430.
(13) Kim, J.; Park, K. Y.; Park, I.; Yoo, J. K.; Seo, D. H.; Kim, S. W.; Kang, K. *J. Electrochem. Soc.* **2012**, *159*, A55−A59.
(14) Chen, G.; Richardson, T. J. *J. Power Sources* **2010**, *195*, 1221−1224.
(15) Delacourt, C.; Poizot, P.; Morcrette, M.; Tarascon, J. M.; Masquelier, C. *Chem. Mater.* **2004**, *16*, 93−99.
(16) Truong, Q. D.; Devaraju, M. K.; Tomai, T.; Honma, I. *ACS Appl. Mater. Interfaces* **2013**, *5*, 9926−9932.
(17) Bramnik, N. N.; Nikolowski, K.; Baehtz, C.; Bramnik, K. G.; Ehrenberg, H. *Chem. Mater.* **2007**, *19*, 908−915.
(18) Wizansky, A. R.; Rauch, P. E.; Disalvo, F. J. *J. Solid State Chem.* **1989**, *81*, 203−207.
(19) Chen, G.; Song, X.; Richardson, T. J. *Electrochem. Solid-State Lett.* **2006**, *9*, A295−A298.
(20) Weichert, K.; Sigle, W.; van Aken, P. A.; Jamnik, J.; Zhu, C.; Amin, R.; Acartürk, T.; Starke, U.; Maier, J. *J. Am. Chem. Soc.* **2012**, *134*, 2988−2992.
(21) Malik, R.; Abdellahi, A.; Ceder, G. *J. Electrochem. Soc.* **2013**, *160*, A3179−A3197.
(22) Huang, Y.; Fang, J.; Omenya, F.; O'Shea, M.; Chernova, N. A.; Zhang, R.; Wang, Q.; Quackenbush, N. F.; Piper, L. F. J.; Scanlon, D.; Whittingham, M. S. *J. Mater. Chem. A* **2014**, *2*, 12827−12834.
(23) Park, J.; Oh, S.; Sun, Y.; Myung, S. *J. Power Sources* **2014**, *256*, 479−484.
(24) Toby, B. H. *J. Appl. Crystallogr.* **2001**, *34*, 210−213.
(25) Larson, A. C.; Von Dreele, R. B. *General Structure Analysis System (GSAS)*; Los Alamos National Laboratory Report LAUR 86-748; Los Alamos National Laboratory: Los Alamos, NM, 2000.
(26) Ravel, B.; Newville, M. *J. Synchrotron Radiat.* **2005**, *12*, 537−541.
(27) Hung, I.; Zhou, L.; Pourpoint, F.; Grey, C. P.; Gan, Z. *J. Am. Chem. Soc.* **2012**, *134*, 1898−1901.
(28) Chen, J.; Vacchio, M.; Wang, S.; Chernova, N. A.; Zavalij, P.; Whittingham, M. S. *Solid State Ionics* **2008**, *178*, 1676−1693.
(29) Pouchot, A.; Durif, A. *Topics in Phosphate Chemistry*; World Scientific: Singapore, 1996.
(30) Kim, J.; Middlemiss, D. S.; Chernova, N. A.; Zhu, B. Y. X.; Masquelier, C.; Grey, C. P. *J. Am. Chem. Soc.* **2010**, *132*, 16825−16840.

DOI: 10.1021/acs.inorgchem.6b00089
Inorg. Chem. 2016, 55, 4335−4343